Acta Materialia 134 (2017) 155–166

Contents lists available at ScienceDirect

Acta Materialia

journal homepage: www.elsevier.com/locate/actamat

Full length article

Multilevel hierarchy in bi-material lattices with high specific stiffness and unbounded thermal expansion

Hang Xu, Amr Farag, Damiano Pasini*

Department of Mechanical Engineering, McGill University, 817 Sherbrooke St. West, Montreal, QC H3A 0C3, Canada

ARTICLE INFO

Article history:
Received 8 February 2017
Received in revised form
10 May 2017
Accepted 27 May 2017
Available online 30 May 2017

Keywords:
Thermal expansion tunability
Thermoresponsive materials
Cellular solids
Composites
Mechanical properties

ABSTRACT

Dual-material concepts that expand or contract as desired upon changes in temperature exist but have their limitations. One upon which we focus here is the trade-off caused by the inherent thermo-elastic coupling that they feature, a condition that makes desired changes in thermal expansion penalize elastic stiffness, and vice versa. In this paper, we present hierarchical bi-material lattices that are stiff and can be designed to attain a theoretically unbounded range of thermal expansion without (i) impact onto elastic moduli and (ii) severe penalty in specific stiffness. Through a combination of theory, numerical simulations and experiments, we demonstrate the thermomechanical performance of eight hierarchical lattices, including two fractal-like hierarchical lattices with self-repeating units that are built from dual-material diamond shapes with low and high coefficients of thermal expansion (CTE). Results show that the achievable range of CTE can be enlarged by 66% through the addition of one order of hierarchy only, and that for a given CTE range the specific stiffness can be at least 1.4 times larger than that of existing stretch-dominated concepts. The concepts here introduced can open up new avenues towards multifunctional devices and structurally efficient materials with simultaneously customized thermal expansion and mechanical properties.

1. Introduction

Architected materials can be designed to elicit extreme mechanical properties, often beyond those of existing solids [1]. They are very appealing for use in several fields of engineering including aerospace, automotive and biomedical [2–4]. In these applications, the target to maximize might be either structural, through attaining for example minimum mass at maximum stiffness [5,6], or functional, such as thermal dimension control [2], heat transfer [7], band gaps [8], mechanical biocompatibility [9], and others [1]. For lightweight structural applications, high stiffness is desired for preserving the structural integrity and resisting a variety of loading conditions. In contrast, high compliance is required to adapt under other loading conditions for more functional applications, such as energy absorption [10]. For functional applications, the coefficient of thermal expansion (CTE) has been the recent focus of intense research [11,12] aiming at obtaining large positive, zero or negative CTE via material architecture tuning.

The design freedom to adjust thermal expansion is particularly advantageous in a large assortment of applications. On one hand, in extreme thermal environments, sensitive applications that require very fine precision, such as satellite antennas, space telescopes, and large array mirrors [4,13], call for materials with zero CTE so as to avoid undesired thermal deformation. On the other hand, there are other applications requiring materials with large positive or negative CTEs. These materials must induce responsive and desirable deformations under given changes in temperature [14], often, but not always, dictated by the surrounding environment, such as in morphing and adaptive structures [15,16], as well as MEMS [17]. The potential of periodic architected materials is also appealing because their repeating cell can be designed to concurrently maximize multiple performance requirements, notably structural and functional. Among many, examples of multifunctional lattices include those developed for aerospace components that can maintain precise dimensional tolerances under large temperature fluctuations and specific stiffness requirements [2,18].

This paper focuses on multifunctional lattices designed with the goal of providing unique control of thermal expansion and structural performance, at levels currently unmet by existing concepts. As with previous works [2,11,18–23], we deal with material architectures made of two materials, which can be designed to

* Corresponding author.
E-mail address: damiano.pasini@mcgill.ca (D. Pasini).

http://dx.doi.org/10.1016/j.actamat.2017.05.059
1359-6454/

compensate the mismatched thermal deformation generated by each of the two materials. If exploited, this strategy enables the attainment of an overall thermal deformation that can be large positive, zero or large negative. Since dual material architectures achieve a tunable CTE through a purely mechanical, and thus temperature-independent, mechanism [4], their CTE is extremely dependent on the unit cell architecture and on the difference in CTE of their constituent solids [12,18]. To assess the potential of a given architected material in providing a range of CTE values via tailored selection of its material constitutes and its cell topology, we need a quantitative metric. CTE tunability, (ΔCTE) has been recently used [23] to measure the maximum range of CTE values that a concept can achieve upon changes of its unit cell geometry from a given pair of materials. Whereas a single material has only one CTE value, hence no ΔCTE, the CTE of dual material concepts can be adjusted by geometric manipulation of the building block with the result of obtaining a range of CTE values. The difference between the minimum and maximum CTE that an architected material can offer is defined as ΔCTE. For a given concept, a large ΔCTE indicates ample freedom to tune the unit cell geometry, an asset that can release the dependence on the CTE ratio of the constituents (see Supplementary Material A).

Several dual-material concepts have been proposed in the literature, most notably by Lehman and Lakes [19,24], Steeves et al. [18], Hopkins et al. [25], Jefferson et al. [20], Sigmund et al. [22], and Xu et al. [23]. A number of these concepts, such as Lakes concept [26], while successful in demonstrating theoretically unbounded CTE tunability, feature a trade-off in structural efficiency [27]. The compromise between them emphasizes an inherent coupling between mechanical properties and thermal properties. This is typical of existing dual-materials concepts (See Supplementary Material A), for which CTE tailoring through architecture manipulation may result in severe reduction of mechanical performance. For example, some existing concepts show that the desired flexural deformation that a large CTE tunability would require is generally antagonist to the high specific stiffness that is distinctive of a structurally efficient architecture. This indicates that preserving high specific stiffness is in conflict with the need of enhancing ΔCTE, as manifest in stretch-dominated unit cells constructed by dual-material triangle (2D) or tetrahedron (3D), which offer a remarkable structural performance [2,18], but cannot achieve the sizeable CTE tunability of bend-dominated architectures [11,26]. Hence, the main issue we want to address in this paper: how to reduce the penalty that an increase in ΔCTE will generate on the elastic properties, so as to obtain the best compromise out of them.

This work proposes hierarchical lattice materials which feature enhanced CTE tunability regardless of the choice of the constituent solids, and enable thermal expansion control without incurring in severe loss of structural performance. Structural hierarchy is not new and for a long time now has been recognized as one crucial factor governing high stiffness, strength, and toughness in both natural and bio-inspired materials [28–30], and even more recently in the field of thermal expansion [19]. However, what has not been so far explored yet is how to exploit it to, first, amplify CTE tunability in architected materials, and then to decouple physical properties that are in conflict. The method adopted in this paper, as explained in Section 2, combines solid mechanics theory, finite element simulations and experiments on proof-of-concept lattices. The results presented in Section 3 demonstrate that initially coupled properties can be individually tuned in distinct hierarchical orders to obtain large CTE tunability without sensible loss in structural performance. Section 4 discusses the concept performance by drawing a comparison with a set of existing architected materials that are stretch and bend dominated.

2. Methodology

Our focus here is on bi-material unit cells (Fig. 1) with high and low CTE, which are used to build hierarchical lattices (HL) including those made of self-repeating unit cells, i.e. fractal-like hierarchical lattices (fractal-like HL) and hierarchical lattices which feature at least two unit cells with different topologies, thus making the hierarchical lattice of a hybrid-type (hybrid-type HL) (Fig. 2). The following provides closed-form expressions and computational results of their thermomechanical properties, along with details on sample fabrication and CTE testing.

2.1. Unit cell model with a bi-material diamond shape

Fig. 1a-I shows the diamond that can attain a low-CTE performance (LD). Upon a uniform increase of temperature, red (α_{s1}) and blue (α_{s2}) elements in a LD deform at different rates, visualized in Fig. 1a-II as unbonded for explanation purpose. Fig. 1a-II displays the height increase, ΔH_{l1}, caused solely by thermal expansion in the blue elements. In the final configuration (Fig. 1a-III), rigid connections at the nodes cause a higher expansion in the red horizontal bar that turns the blue struts. As a result, the top vertex of the diamond springs back by ΔH_{l2}, a displacement that if desired can be conveniently designed to compensate ΔH_{l1}. By harnessing the values of α_{s1} and α_{s2}, or the skewness of the blue elements, θ, the CTE of a LD can be tuned to zero, or even negative, in the y-direction. Similarly, Fig. 1b-I shows the complementary version of the diamond in Fig. 1a-I, where the switched material distribution yields a high-CTE diamond (HD). In Fig. 1b-II, the expansion of the red elements bring about a height increase, ΔH_{h1}, and a width-wise gap, ΔW_h, which would appear if the blue bar, which exhibits less expansion, were visualized as unconnected. Also in this case, rigid connections (Fig. 1b-III) would compensate the visualized horizontal gap, ΔW_h, by a height increase of ΔH_{h2}, adding on to ΔH_{h1}, and this value of ΔH_{h2} can also be tuned by manipulating α_{s1}, α_{s2} and θ. From this explanation, we gather that the CTE in the y-direction depends on the thermal expansion ratio of the constituent materials, $\xi = \alpha_{s2}/\alpha_{s1}$, and the skewness angle, θ. If θ is given, the smaller the ξ, the lower (for LD) or higher (for HD) the CTE [18]; hence the greater the CTE distinction of the constituent solids, the higher the CTE tunability.

We now examine the general case of a LD (Fig. 1a-I) with an arbitrary skew angle, θ, and we derive its Young's moduli, from which those for HD can also be easily obtained. A small thickness ratio is considered, $t/l < 1/8$, that gives LD a low relative density, ρ^*/ρ_s, which is defined as the ratio of its real density over the density of the solid. For a generic dual-material unit cell, the relative density can be expressed as a function of the volume fractions of the constituents (Supplementary Material B), and more specifically for a LD (details in Supplementary Material C) can be written as:

$$\frac{\rho^*}{\rho_s} = \frac{\cos\theta + 2}{\sin\theta}\frac{t}{l} \tag{1}$$

Using structural mechanics [31], the in-plane Young's moduli can be derived as (Supplementary Material C):

$$\frac{E_y^*}{E_{s2}} = \left(\frac{1}{2\sin^3\theta} + \frac{E_{s2}/E_{s1}}{\tan^3\theta}\right)^{-1}\frac{t}{l} \tag{2}$$

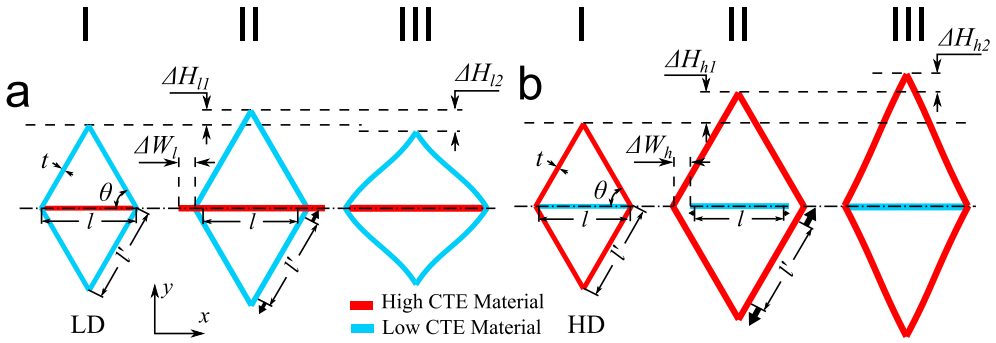

Fig. 1. Deformation of a unit cell in a diamond shape with low, LD (a-I), and high, HD (b-I), CTE, strut thickness t, horizontal bar length l, sloped bar length l', and skew angle θ. (II) Deformation of hypothetically unconnected elements and their corresponding dimensional changes. (III) Actual deformation of rigidly connected elements along with change in dimensions due to rigid nodal connectivity.

$$\frac{E_x^*}{E_{s2}} = \frac{E_{s1}/E_{s2}}{\tan\theta}\frac{t}{l} \tag{3}$$

where E_{s1} and E_{s2} are the Young's modulus for solid materials 1 and 2, respectively. We note that although Eqs. (2) and (3) are valid for a defect-free lattice in a fully undeformed state, the thermal deformation and fabrication imperfections, which are less than ±1% of the bar length deviation, will not significantly reduce the elastic moduli (no more than 5% [32]). Even under the largest achievable temperature changes considered in this article ($\Delta T = 50\,^{\circ}$C), the thermal deformation remains small, thereby causing no significant impact on the elastic moduli.

Since the thermal expansion mismatch between the constituent materials cause bar bending, the effective CTE in the y-direction can be written (Supplementary Material C) as:

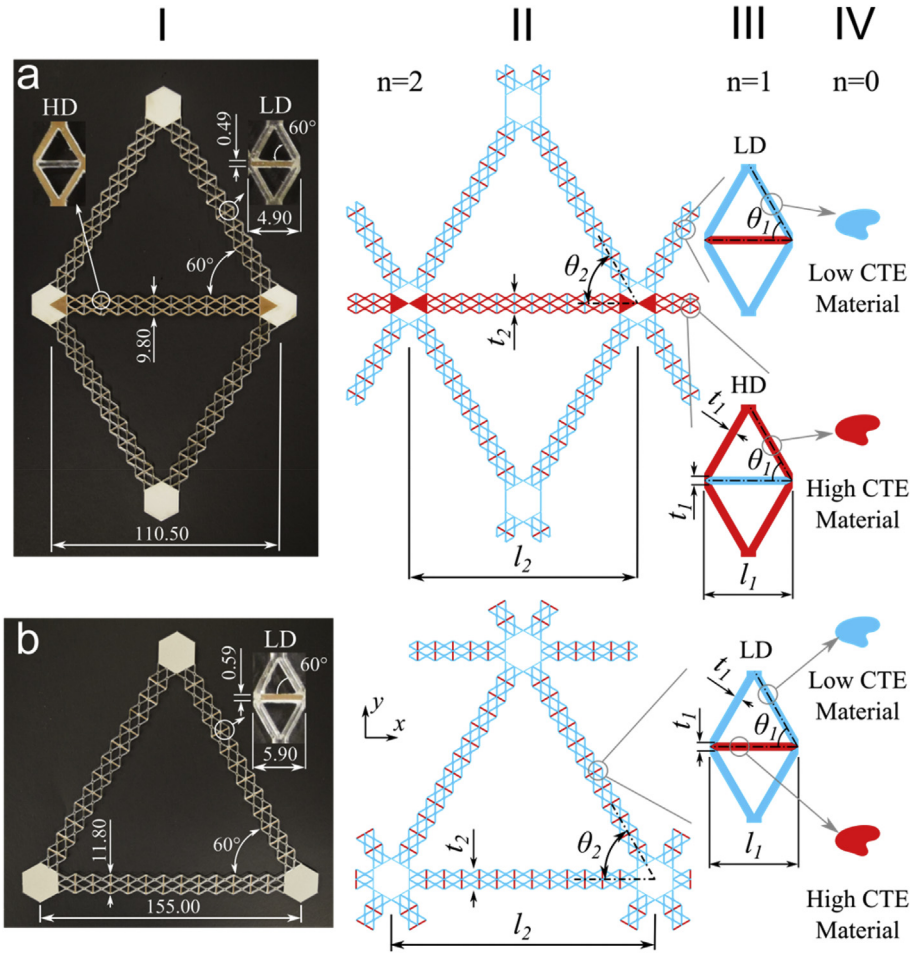

Fig. 2. Multiscale lattices with second-order hierarchy (n = 2). (a-I) Fabricated fractal-like HL with low-CTE, (b-I) hybrid-type HL with low-CTE with specified dimensions denoted in mm. (a-II) and (b-II) geometric models of second-order hierarchy with cell-wall thickness, t_2, and length, l_2. (a-III) and (b-III) first order unit cell models with low- and high-CTE shaped-diamond, i.e. LD and HD, and their respective cell-wall thickness, t_1, and length, l_1. θ_n with $\theta_n \in (0, 90^{\circ})$ is the angle between the inclined cell wall and the x-direction. (a-IV) and (b-IV) constituent materials colour-coded to illustrate low and high CTEs. All lattices are planar with prismatic units of identical out-of-plane thickness.

$$\alpha_y^* = \alpha_{s2} + \frac{(\cos\theta/2 - (8\cos\theta(t/l)^2)^{-1})(\alpha_{s1} - \alpha_{s2})}{\frac{\sin^2\theta}{8\cos^3\theta(t/l)^2} + \frac{\cos\theta}{2} + \frac{E_{s2}}{E_{s1}}} \tag{4}$$

Similarly in the x-direction, the effective CTE is (Supplementary Material C):

$$\alpha_x^* = \alpha_{s1} - \frac{(E_{s2}/E_{s1})(\alpha_{s1} - \alpha_{s2})}{\frac{\sin^2\theta}{8\cos^3\theta(t/l)^2} + \frac{\cos\theta}{2} + \frac{E_{s2}}{E_{s1}}} \tag{5}$$

Eq. (4) can be simplified as:

$$\alpha_y^* = \alpha_{s2} + k_{CTE}(\alpha_{s1} - \alpha_{s2}) \tag{6}$$

where $k_{CTE} = (\cos\theta/2 - (8\cos\theta(t/l)^2)^{-1})(\sin^2\theta/(8\cos^3\theta(t/l)^2) + \cos\theta/2 + E_{s2}/E_{s1})^{-1}$ has always a negative value. The LD and HD cases can be specified by the difference in values of the two solid CTEs. If $\alpha_{s1} > \alpha_{s2}$, α_y^* is less than the lowest CTE of the two solids (i.e. α_{s2}), thus representing LD (Fig. 1a-I). On the other hand, if $\alpha_{s2} > \alpha_{s1}$, then α_y^* is larger than the highest CTE - in this instance α_{s2} - which corresponds to the HD case (Fig. 1b-I).

In Eqs. (4) and (5) above, the effective CTE is also governed by the geometric parameters of the lattice, namely t/l and θ. The stiffness can also be expressed similarly to the CTE, since they are contingent on the same set of geometric parameters (i.e. t/l and θ in Eqs. (2) and (3)). From this, it is evident that a change of this set of parameters would make both the CTE and stiffness vary, as further demonstrated in Supplementary Material A. How to avoid this thermo-elastic coupling is illustrated later in this section, after we first explain below how to enlarge ΔCTE in architectures made of any pair of materials.

The LD and HD unit cells introduced above can be used as building blocks to create multiscale self-repeating lattices (fractal-like HL) with potentially unbounded range of CTE without severe penalty in specific stiffness. This can provide better trade-off between thermal and mechanical performance. This performance is achieved with neither change of their constituent materials nor manipulation of their skew angles. The underlying principle here is that by replacing the solid constituents with unit cells with higher (HD) and lower (LD) CTE values than those of their base materials, we amplify ΔCTE. Fig. 2a shows a low-CTE example of fractal-like HL with two hierarchical orders, each constructed through the tessellation of LD and HD with prescribed internal angle $\theta = 60°$. The reverse performance case, i.e. higher CTE, can be obtained by a switch of HD and LD positions. Higher orders can be introduced to reduce or enlarge the effective CTE in desired directions with high structural efficiency (E/ρ) originating from the stretch-dominated cell this fractal-like HL is built from.

For the analysis, we consider the general case of n^{th} order fractal-like HL of density ρ_n^*, effective Young's modulus E_n^*, and effective CTE α_n^*. The cell walls consist of LD and HD cells of density, ρ_{n-1}^*, effective Young's modulus, E_{n-1}^*, and effective CTE, α_{n-1}^*. The skew angle θ is given and common to all hierarchical orders, whereas the thickness ratios t_i/l_i are different. The relative density for the general case of fractal-like HL with n orders is:

$$\frac{\rho_n^*}{\rho_s} = \left(\frac{\cos\theta + 2}{\sin\theta}\right)^n \left(\frac{t_n}{l_n}\right)\cdots\left(\frac{t_2}{l_2}\right)\left(\frac{t_1}{l_1}\right) = \left(\frac{\cos\theta + 2}{\sin\theta}\right)^n \prod_{i=1}^{n}\left(\frac{t_i}{l_i}\right) \tag{7}$$

The Young's modulus of the high- and low-CTE fractal-like HL in the y-direction can be expressed as:

$$\begin{cases} \dfrac{E_{l,y,i}^*}{E_{l,y,i-1}^*} = \left(\dfrac{1}{2\sin^3\theta} + \dfrac{E_{l,y,i-1}^*/E_{h,y,i-1}^*}{\tan^3\theta}\right)^{-1}\dfrac{t_i}{l_i} \\ \dfrac{E_{h,y,i}^*}{E_{l,y,i-1}^*} = \left(\dfrac{E_{l,y,i-1}^*/E_{h,y,i-1}^*}{2\sin^3\theta} + \dfrac{1}{\tan^3\theta}\right)^{-1}\dfrac{t_i}{l_i} \end{cases} \begin{pmatrix} 1 \le i \le n, \\ E_{h,y,0}^* = E_{sh}, \\ E_{l,y,0}^* = E_{sl} \end{pmatrix} \tag{8}$$

where h and l represent the high- and low-CTE, respectively, and i represents the hierarchical order, such that $E_{l,y,i}^*$ is the effective Young's modulus of the low-CTE element in the i^{th} order and the y-direction. Their effective CTEs are given by:

$$\begin{cases} \alpha_{l,y,i}^* = \alpha_{l,y,i-1}^* + \dfrac{\left(\dfrac{\cos\theta}{2} - \dfrac{(t_{i-1}/l_{i-1})^{-2}}{8\cos\theta}\right)\left(\alpha_{h,y,i-1}^* - \alpha_{l,y,i-1}^*\right)}{\dfrac{\sin^2\theta}{8\cos^3\theta}\left(\dfrac{l_{i-1}}{t_{i-1}}\right)^2 + \dfrac{\cos\theta}{2} + \dfrac{E_{l,y,i-1}^*}{E_{h,y,i-1}^*}} \\ \alpha_{h,y,i}^* = \alpha_{h,y,i-1}^* + \dfrac{\left(\dfrac{\cos\theta}{2} - \dfrac{(t_{i-1}/l_{i-1})^{-2}}{8\cos\theta}\right)\left(\alpha_{l,y,i-1}^* - \alpha_{h,y,i-1}^*\right)}{\dfrac{\sin^2\theta}{8\cos^3\theta}\left(\dfrac{l_{i-1}}{t_{i-1}}\right)^2 + \dfrac{\cos\theta}{2} + \dfrac{E_{h,y,i-1}^*}{E_{l,y,i-1}^*}} \end{cases} \tag{9}$$

with $1 \le i \le n$, $\alpha_{h,y,0}^* = \alpha_{sh}$, $\alpha_{l,y,0}^* = \alpha_{sl}$, $E_{h,y,0}^* = E_{sh}$, and $E_{l,y,0}^* = E_{sl}$.

The relations above show that fractal-like HL of any hierarchical order possesses anisotropic thermo-elastic properties that are coupled. Isotropic (planar) behaviour can be attained by changing cell shapes among structural order, i.e. by creating hierarchical lattices, with shapes that exhibit isotropy. Below we apply this strategy and consider self-repeating lattices that are shaped at the last order with cell geometry dissimilar than those of the preceding orders, so as to create hybrid-type HL.

Fig. 2b illustrates an example of hybrid-type HL with two levels of hierarchy. A change in unit cell shape, i.e. a triangle, is implemented at $n = 2$ to show how hierarchy can be effective in not only decoupling but also tuning thermo-elastic properties. As opposed to the fractal-like HL in Fig. 2a-I, which contains both LD and HD, in Fig. 2b-I only LD is used at $n = 1$ to create a triangle hierarchical lattice with low-CTE, whereas its high-CTE counterpart can be obtained by swapping the material position. We shape hybrid-type HL at $n = 2$ with a triangle to infer isotropic (planar) mechanical properties and control thermal expansion with LD at $n = 1$. This simple strategy is effective in achieving desired levels of property decoupling which can be readily extended to lattices of higher hierarchical order and beyond CTE and stiffness, such as CTE and strength, CTE and Poisson's ratio, thermal-conductivity and Poisson's ratio, and others.

Let's examine hybrid-type HL with $n = 2$. If the 2^{nd} order consists of LD only (Fig. 2b-I), then its overall effective CTE, α_2^*, is equal to the CTE of LD in the axial direction (y-direction in the current case), which can be simply expressed as $\alpha_2^* = \alpha_{1y}^*$. This shows that α_2^* is not dependent on any changes in geometry at the 2^{nd} order, such that θ_2 and t_2/l_2 have no influence on the effective CTE of the overall hybrid-type HL. However, any geometric changes at the first order, such as the skew angle, will affect not only α_{1y}^* but also the CTE of the overall hybrid-type HL, i.e. α_2^*. With respect to elastic stiffness for hybrid-type HL, the normalized effective Young's modulus E_2^*/E_1^* of the 2^{nd} order, which is mainly a function of unit

cell topology, nodal connectivity, cell wall angle, and relative density, ρ_2^*/ρ_1^*, can be expressed through the wall thickness ratio, t_2/l_2 as:

$$\frac{E_2^*}{E_1^*} = k_2\left(\frac{t_2}{l_2}\right)^q \tag{10}$$

k_2 is a function of the cell topology adopted at the 2nd order of hybrid-type HL; q depends on the cell wall deformation mode of the 2nd order - stretching or bending - and can assume values that depend on the scaling condition applied to the cell wall cross-section [33–35]. If E_1^* is given, the stiffness of the 2nd order is merely a function of the geometry at the 2nd order and any geometric change at this order will not influence the overall CTE of hybrid-type HL.

The thermal and mechanical 2D isotropic behaviour of the hybrid-type HL in Fig. 2b derives from the shape of the unit cell, in this case a triangle. The relevant properties of hybrid-type HL at $n = 1$ are given in Eqs. (1), (2) and (4), and the mechanical properties at $n = 2$ ($\theta_2 = 60°$) in Eqs. (11) and (12). Since the CTE of the last order hybrid-type HL, α_2^*, is equivalent to that of the preceding order, in this example the CTE of LD, or HD for the high-CTE case, the thermomechanical properties of hybrid-type HL are given by:

$$\frac{\rho_2^*}{\rho_1^*} = 2\sqrt{3}\ \frac{t_2}{l_2} \tag{11}$$

$$\frac{E_2^*}{E_{1y}^*} = \frac{2\sqrt{3}}{3}\frac{t_2}{l_2} \tag{12}$$

$$\alpha_2^* = \alpha_{1y}^* \tag{13}$$

To demonstrate CTE tuning that brings no change in the elastic properties of hybrid-type HL, we seek in its first order a set of pairs for the skew angle θ_1 and t_1/l_1 that can satisfy the condition of constant E_{1y}^*. This can be achieved by rearranging Eq. (4) to find the expression of E_{1y}^* that is governed by t_1/l_1 and θ_1, and whose solution provides CTE values at the first order, α_1^*, that change with the skew angle but leave E_{1y}^* unaltered. This strategy preserves the Young's moduli in the second order and allows CTE tuning in the first order. Furthermore, this scheme enables to construct hybrid-type HL with tunable stiffness via changing wall thickness at the second order, t_2/l_2, while keeping the overall CTE α_2^* constant, hence allowing thermo-elastic decoupling.

The explanation given above is of course demonstrative for hybrid-type HL of 2 orders. If $n > 2$ and hybrid-type HL has the triangle at the last (n^{th}) order, the scheme still holds and enables to decouple CTE from elastic stiffness. In this case, the first order to the $(n-1)^{th}$ order are made of low-CTE fractal-like HL; and the relative density and thermo-elastic properties of the highest order can be expressed using Eqs. (11)–(13) by simply replacing 2nd order terms with n^{th} order terms and 1st order with $(n-1)^{th}$ order. The effective properties ρ_{n-1}^*, E_{n-1}^*, and α_{n-1}^* in those general equations can be calculated through Eqs. (7)–(9), respectively.

2.2. Experimental validation

Three sets of experimental validation (Figs. 3–5) for the prediction models presented earlier are performed on laser cut prototypes of hierarchical lattices. Given the scheme presented here is material selection free, a representative pair of materials is chosen to fabricate the samples: Teflon® Polytetrafluoroethylene (PTFE, DuPont, USA), and acrylic plastic (Polymethyl Methacrylate (PMMA), Reynolds Polymer, Indonesia) (materials properties in Table 1). Nevertheless, the experimental validation here provided can be applied to lattices made of any pair of solids including metals, such as Al6061 and Ti-6Al-4V, and for hierarchical orders above 2. The first set of experiments aims at validating the fractal-like HL model that can predict CTE values and its tunability (Eq. (9)), where the low-CTE of a representative lattice is tested in the y-direction. The second set is designed to measure CTE tunability for hybrid-type HL with $n = 2$ (Eqs. (4) and (13)), and the third to demonstrate thermo-elastic properties decoupling (Eqs. (4) and (13)).

Sheets of 1.59 mm thickness of each material were laser cut (TROTEC Laser GmbH, Austria) to build 2nd order fractal-like and hybrid-type HL. Laser cutter was calibrated to provide planar deviations within ±0.05 mm. Bar elements were individually embedded to diamond-shaped cells and epoxy glue (Gel Epoxy Syringe Glue, LePage) was applied to provide adherence between materials. The epoxy glue thickness was about 0.1 mm, 2% of the typical length of a lattice element; the epoxy CTE ($65 \times 10^{-6}/°C$) was similar to the CTE of acrylic, thus providing negligible influence on the CTE measurements of HL samples.

A 3D digital image correlation (DIC) set-up with a temperature controlled heating chamber (See Supplementary Material D for details) was assembled and used to assess the CTE of each set of HLs. In total, 3 sets of DIC experiments were undertaken for a total of 9 tests, 3 for each set. In the first group (Fig. 3), DIC was applied to solid bars of acrylic and 2 fractal-like HLs, one with 1 order of hierarchy and the other with $n = 2$. The skew angle ($\theta = 60°$) as well as the wall thickness ratio (about $t/l = 0.1$) of the fractal-like HL were kept identical. The joints were shaped in hexagons to preserve strut connectivity (six) at each node. The second set (Fig. 4) features DIC results for 2nd order hybrid-type HL samples with varying skew angles (55°, 60° and 65°) and hexagonal nodes of dimensions identical to those of the first set. To prove CTE tunability of hybrid-type HL for constant Young's modulus, E_{y1}^*, the geometry of the three hybrid-type HL samples was kept identical with the exception of their skew angles, θ_1, and wall thickness, t_1, in the first order. The last set of samples in Fig. 5, second order hybrid-type HL, were built with varying strut thickness to assess the impact of t_2/l_2 on their effective CTE. Here the geometric parameters of all samples were kept identical except the thickness ratio of the second order ($n = 2$) chosen as the only variable. The number of LD along the thickness direction varied from $M = 1$ to $M = 3$ as shown in Fig. 5a, b, and c.

Table 1
Predicted and experimentally measured CTE values ($\times 10^{-6}/°C$) for solid materials.

Material	Measured CTE (DIC)	Measured CTE (TMA Q400)	CTE provided by the supplier	Difference (%)	Young's Modulus (GPa)	Density (g/cm^3)
Acrylic (Low CTE component)	67.0 ± 0.5	–	69.0	2.9%	3.2	1.2
Teflon® PTFE (High CTE component)	123.0 ± 0.9	–	120.0	2.5%	0.475	2.2
Al6061	22.6 ± 0.4	23.0	–	1.7%	-	-

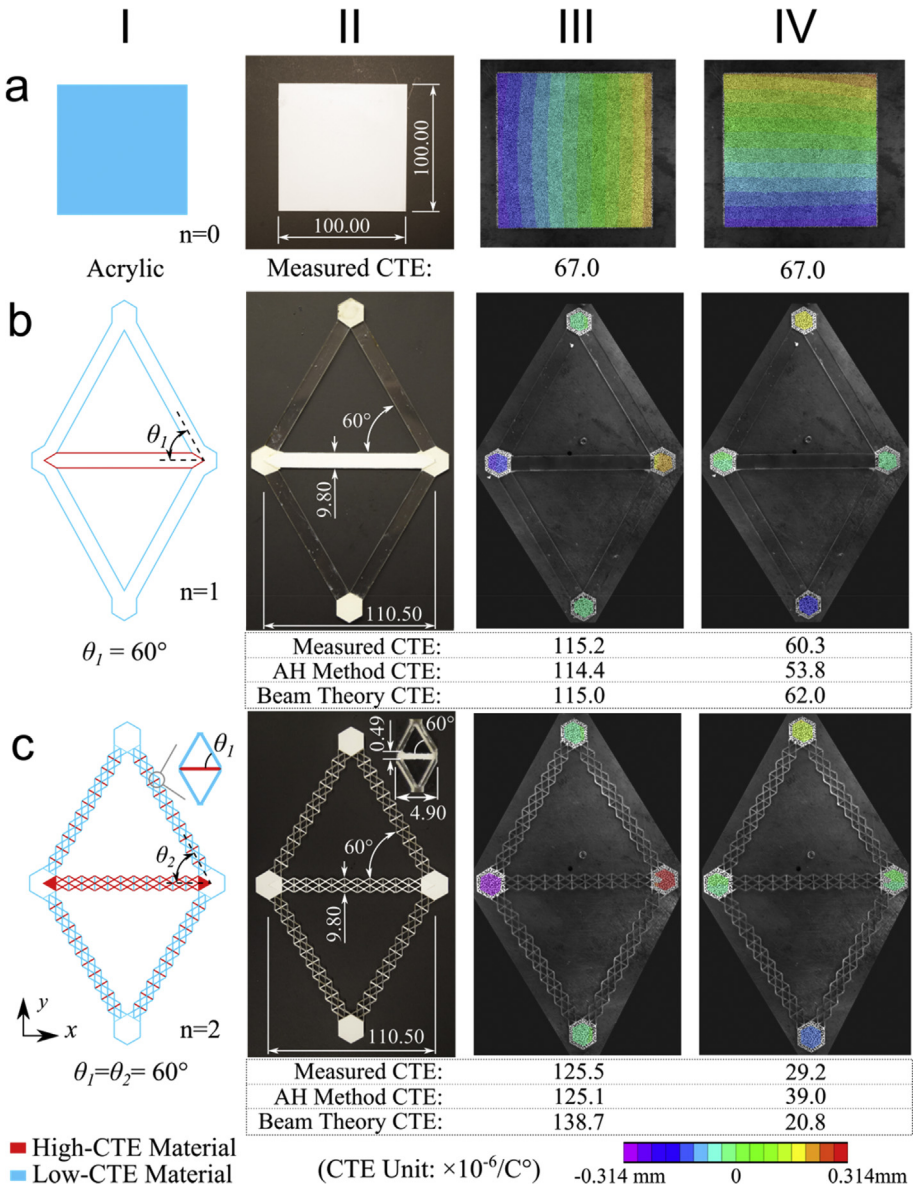

Fig. 3. Thermal experiment of fractal-like HL with: $n = 0$ (a); $n = 1$ (b); and $n = 2$ (c), and thermal deformation field shown in column (III) for x-direction and column (IV) for y-direction. To perform DIC, black and white speckles were applied randomly and uniformly across the nodes to each hybrid-type and fractal-like HL samples, for thermal displacement measurements. Columns (I) and (II) illustrate respectively initial configurations for designed and fabricated samples. Obtained CTE values along with theoretical and simulated values are summarized along their corresponding columns. Computational values are obtained via asymptotic homogenization.

All samples were tested five times through the thermal cycle to ensure test repeatability, and on each occasion the thermal displacement was measured to provide statistical context to the results.

Testing temperature was monitored and managed from 25 °C to 75 °C through a PID (proportion-integration-differentiation) controller (CN7800, Omega, US). DIC system calibration ensured an epipolar projection error below 0.01 pixels, i.e. the average error between the position where a target point was found in the image and the theoretical position where the mathematical calibration model located the point. A CCD (charge coupled device) camera (PointGrey, Canada) was used to focus on an area of 240 × 200 mm^2 with a resolution of 2448 × 2048 pixels; based on the image resolution, any deformation smaller than 0.98 μm (0.01 pixels) was merged by the epipolar projection error. Finally the accuracy of the whole testing system was verified with measures taken from a commercial thermomechanical analyzer, TMA Q400 (TA Instr., US).

3. Results

3.1. System calibration

The testing system was calibrated on three solid materials, Al6061, acrylic and PTFE. Table 1 shows a comparison of their measured and predicted mean CTE along with their standard deviations, with errors below 3%. The epipolar projection error is at 0.98 μm, which governs the smallest measured CTE value of the samples, i.e. 0.27 × 10^{-6}/°C. The low magnitude of these errors warrants the required accuracy for the DIC system used in this work.

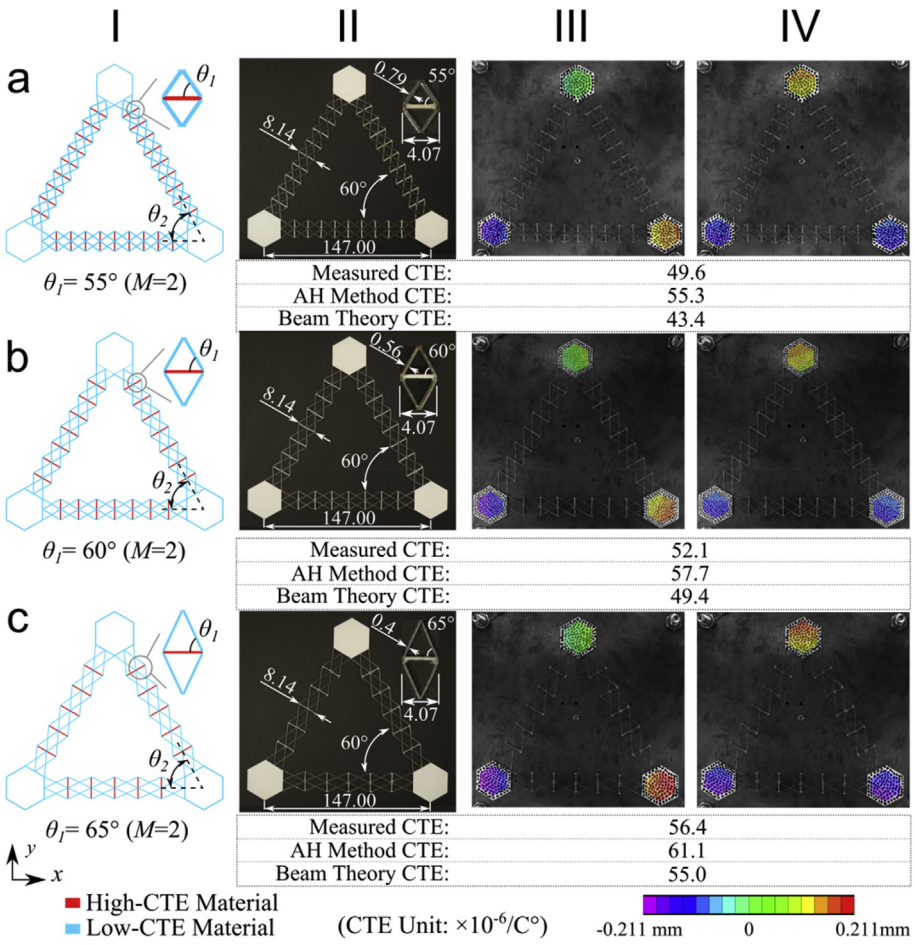

Fig. 4. Thermal experiment of hybrid-type HL with skew angles of 55° (a), 60° (b), and 65° (c) and thermal deformation field shown in column (III) for *x*-direction and column (IV) for *y*-direction. Columns (I) and (II) illustrate respectively initial configurations for designed and fabricated samples. Obtained CTE values along with theoretical and simulated values are summarized along their corresponding columns. Computational values are obtained via asymptotic homogenization.

3.2. Testing results

Fig. 3a-III and IV show thermal deformation maps for the solid material, acrylic, in both *x*- and *y*-directions, respectively. The tested CTE is observed isotropically in all directions in the 2D plane. While their thermal deformation is shown in Figs. 3–5-III and IV in both *x*- and *y*-directions, mean CTE from testing are summarized in Table 2, along with their standard deviation and CTE predictions. The error associated with testing results only go as high as 5%, and the difference between tests and the computational values obtained via asymptotic homogenization (AH) (see Supplementary Material E) are generally within 10% error, with the exception of fractal-like HL ($n = 2$) sample, where the amplified low-CTE behaviour also amplifies the deviation between both results.

Fig. 3b-IV illustrates that LD (Fig. 3b-I, $n = 1$ with $\theta = 60°$) without structural hierarchy can reduce the CTE along the *y*-direction from 67.0 $\times$ 10^{-6}/°C ($n = 0$, i.e. the component material, acrylic, as shown in Fig. 3a-I) to 60.3 $\times$ 10^{-6}/°C. However, for increasing hierarchical order, fractal-like HL (Fig. 3c-I, $n = 2$) can further reduce the effective CTE in the *y*-direction to 29.2 $\times$ 10^{-6}/°C, result obtained with no change in material selection nor skew angle. By adding hierarchical orders from $n = 1$ to $n = 2$, fractal-like HL shows a CTE tunability up to 31.1 $\times$ 10^{-6}/°C. Fig. 4-III and IV show for hybrid-type HL the decrease of the effective CTE from 56.4 $\times$ 10^{-6}/°C ($\theta_1 = 65°$) to 49.6 $\times$ 10^{-6}/°C ($\theta_1 = 55°$), which emphasizes a much smaller CTE tunability (6.8 $\times$ 10^{-6}/°C) in comparison with adding hierarchical orders (31.1 $\times$ 10^{-6}/°C). The combination of varying skew angles and adding hierarchical orders appears to be proficient in tuning the effective CTE. For the last set of specimens, however, the effective stiffness relative to a hybrid-type HL with $M = 1$ is expected to double for $M = 2$ and triple for $M = 3$; the overall effective CTE displays a tendency of remaining constant around 53 $\times$ 10^{-6}/°C. These results experimentally show that thermo-elastic properties can be decoupled in hybrid-type HL, as explained in more detail in the following section.

3.3. Model predictions

Fig. 6a illustrates the CTE values for low- and high-CTE fractal-like HL in the *y*-direction as a function of hierarchical order. Each of the plotted lines, obtained from Eq. (9), represents CTE values for a given skew angle, θ, and starts from $n = 0$, solid materials, through $n = 1$, the HD and LD, followed by fractal-like HLs with increasing hierarchical order $n \geq 2$. We recall that these predictions represent discrete values of CTE, each obtained for a given n, although the trends are shown as continuous to ease their interpretation within each figure. Assuming the CTE of PTFE and acrylic as the high and low CTE values, respectively, we observe that as the order increases from 0 to 1, the effective CTE of HD is higher than that of PTFE, whereas the CTE of the LD is lower than that of acrylic. The gap between these two CTE spectra, i.e. LD and HD, taking $\theta = 60°$ as an example, enlarges from 56 $\times$ 10^{-6}/°C (initial gap between solid

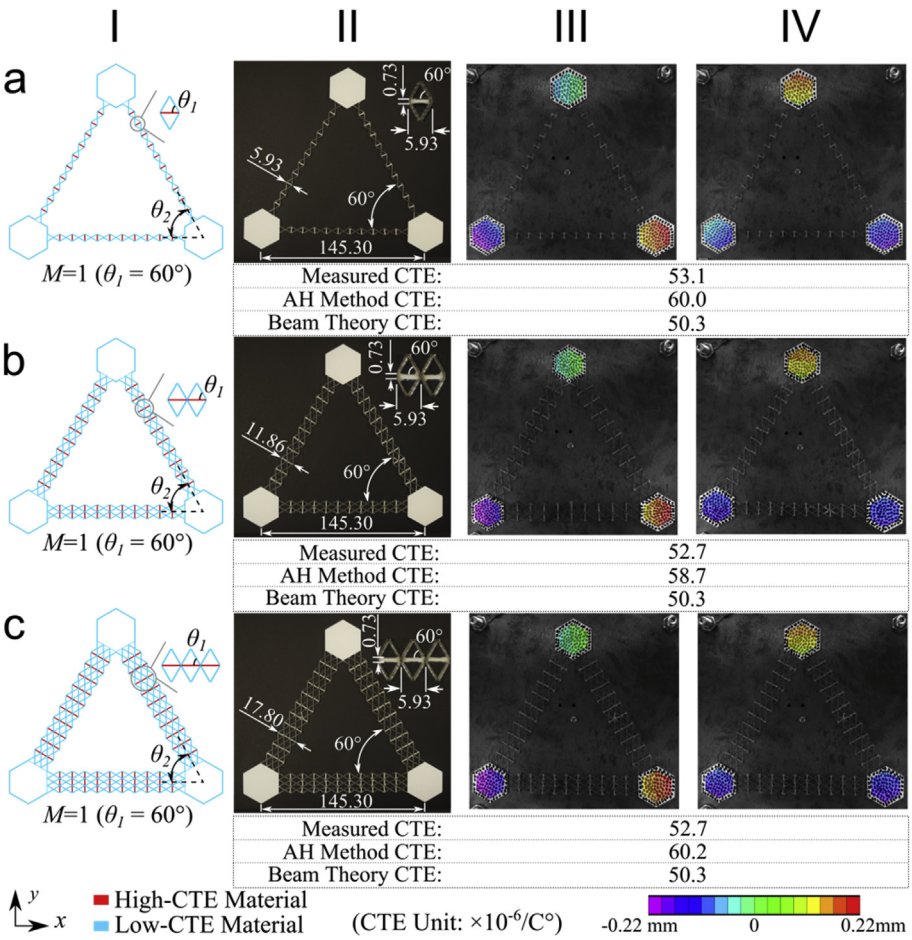

Fig. 5. Thermal experiment of hybrid-type HL with wall layers of $M = 1$ (a); $M = 2$ (b); and $M = 3$ (c) and thermal deformation field shown in column (III) for x-direction and column (IV) for y-direction. Columns (I) and (II) illustrate respectively initial configurations for designed and fabricated samples. Obtained CTE values along with theoretical and simulated values are summarized along their corresponding columns. Computational values are obtained via asymptotic homogenization.

materials) to 93 × 10^{-6}/°C, meaning an increase of 165% in ΔCTE. As the order changes from 1 to 2, the gap increases even more drastically to 154.7 × 10^{-6}/°C (275% of the initial gap) and larger once more from order 2 to 3, reaching 257.3 × 10^{-6}/°C (460% of the initial gap). CTE tunability (ΔCTE) increases with the order of hierarchy, so as to theoretically approach an unbounded value for unlimited n.

We also note the shaded region in Fig. 6a, where the lattice collapses to a by-layer laminate. This concept can cover CTE values between the CTEs of the constituent solids by changing their layer thickness ratio. Furthermore, Fig. 6b illustrates structural efficiency - a metric expressed here as the ratio of the specific stiffness of the lattice to that of the solid materials - in the y-direction of low- and high-CTE fractal-like HL versus hierarchical order. For normalization purposes, solid acrylic (blue in figure) is considered as benchmark with 100% structural efficiency. With the increase of hierarchical order, the structural efficiency of fractal-like HL decreases. This is expected as stretch dominated lattices become more compliant with higher order of hierarchy, but nevertheless this drop is less than that of bend dominated lattices [29]. Another insight that we gain from Fig. 6a and b is that the thermo-elastic properties of fractal-like HL are coupled, and CTE changes as structural efficiency does. How to avoid this coupling is shown below where results obtained from models described in Section 2 are presented.

Fig. 6c and d shows the predicted CTE and structural efficiency for hybrid-type HL as a function of the hierarchical order and the

Table 2
Predicted and experimentally measured CTE values for fractal-like and hybrid-type HL (σ_x and σ_y indicate standard deviation).

Sample	Predicted CTE (Beam Theory, ×10^{-6}/°C)		Measured CTE (×10^{-6}/°C)		Error	
	x	y	$x \pm\sigma_x$	$y \pm\sigma_y$	x	y
Fractal-like HL (n=1)	115.0	62.0	115.2 ± 0.3	60.3 ±2.4	0.2%	2.8%
Fractal-like HL (n=2)	138.7	20.8	125.5 ± 1.3	29.2 ±0.9	10.5%	28.8%
Hybrid-type HL (55°, M=2)	43.4		49.6 ± 1.3		12.5%	
Hybrid-type HL (60°, M=2)	49.4		52.1 ± 0.6		5.2%	
Hybrid-type HL (65°, M=2)	55.0		56.4 ± 2.9		2.5%	
Hybrid-type HL (60°, M=1)	50.3		53.1 ± 1.3		5.3%	
Hybrid-type HL (60°, M=2)	50.3		52.7 ± 1.6		4.2%	
Hybrid-type HL (60°, M=3)	50.3		52.7 ± 1.6		4.2%	

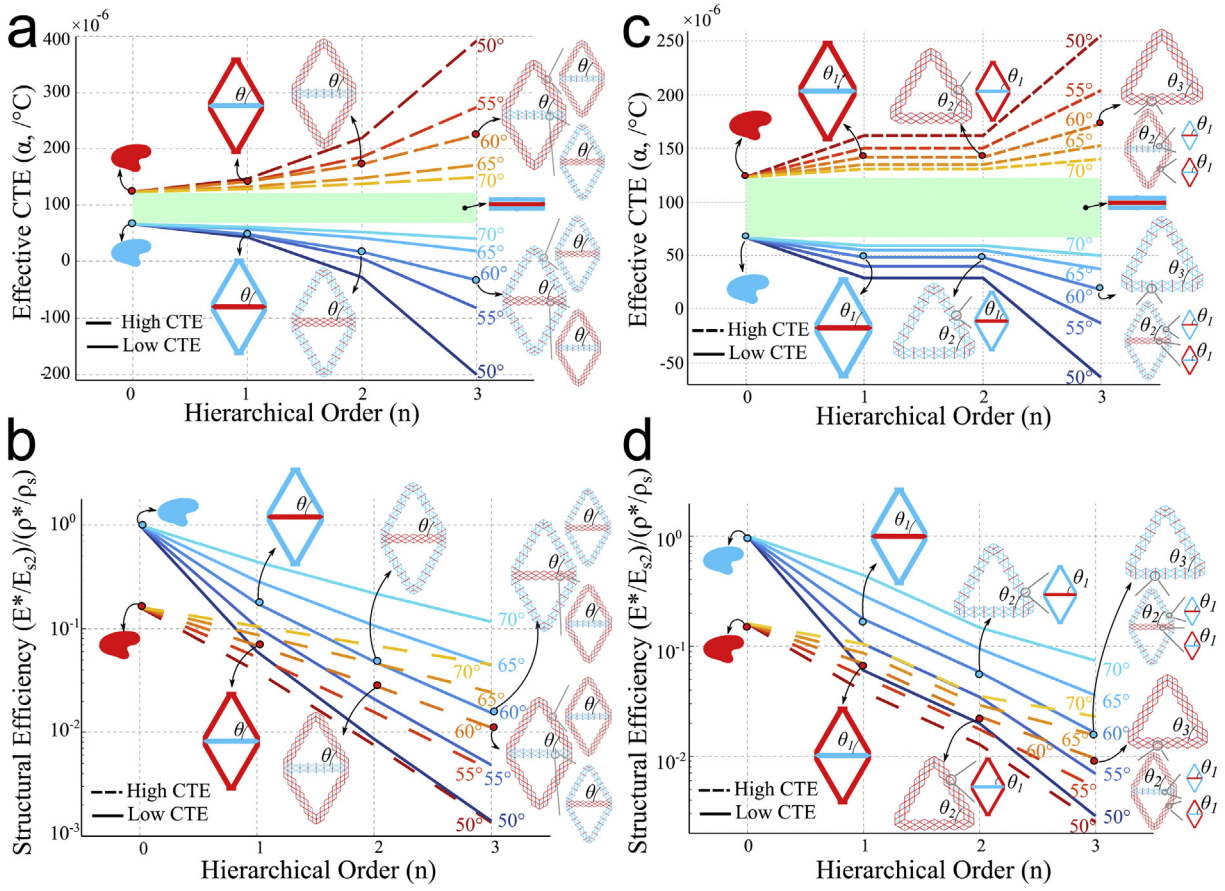

Fig. 6. CTE (a) and structural efficiency (b) of fractal-like HL in the *y*-direction as a function of *n*, the number of hierarchical order; CTE (c) and structural efficiency (d) of hybrid-type HL in the *y*-direction, respectively, with respect to *n*. Lines of given skew angle are visualized for hybrid-type HL and fractal-like HL, and shaded regions (green) in (a) and (c) are depicted to represent by-layer laminates of solid materials ($\theta = 0$). CTE trends shown as continuous connect discrete values calculated via the models presented in Section 2. (For interpretation of the references to colour in this figure legend, the reader is referred to the web version of this article.)

skew angle, θ_1, in the range $50° - 70°$, which is representatively chosen here to visualize the effect of varying skewness. In Fig. 6c, the first order ($n = 1$) allows some degree of CTE tailoring with a gap increase between the low and high CTE spectra from 56×10^{-6}/°C to 93×10^{-6}/°C. With the addition of the second order ($n = 2$), this time hybrid-type HL, as opposed to fractal-like HL, allows stiffness modulation without thermal expansion variation. Hence CTE remains insensitive, i.e. ΔCTE between the first two orders is constant, despite a drop of structural efficiency.

The trends shown in Fig. 6c and d between $n = 1$ and $n = 2$ are now used as an example to show how hybrid-type HL can be effective in decoupling thermal and mechanical properties. To do so, we first show that CTE and Young's modulus for LD are inherently coupled and hence no independent tuning is possible. This is shown in Fig. 7a and b where Eqs. (1)–(5) are plotted in dash style along with results obtained from AH (continuous style), here included to provide a further element of validation to the analytic models presented therein. Fig. 7a shows that for prescribed t_1/l_1, a reduction of the skew angle brings a decrease of both the CTE and Young's modulus in the *y*-direction. On the other hand, if the skew angle is given and t_1/l_1 varies (Fig. 7b), both the CTE and Young's modulus in the *y*-direction show a monotonic increase for rising relative density. Hence Fig. 7a and b visualize the thermo-elastic coupling that exists in diamond lattices. In the next step, we show separate property tuning through hybrid-type HL. Fig. 7c and d shows results for CTE and Young's modulus obtained from Eqs. (12) and (13) for hybrid-type HL of two orders (Fig. 2b-I). Also in this case, results from closed-form expressions are reported along with those obtained computationally via AH. Fig. 7c shows that a changed θ_1 in the first order of hybrid-type HL enables CTE tuning for both orders, while causing no impact in the Young's modulus, as shown by its unchanging trend. Likewise in the mechanical spectrum, Fig. 7d shows that the effective Young's modulus can be varied with relative density with no effect on the CTE. It is the thickness ratio of the second order, t_2/l_2, that, in this case, is the variable empowering the Young's modulus modulation for inviolate values of CTE. Fig. 7, thus, gives a visual summary of model predictions validated through experiments for thermo-elastic coupling, which appears to have been bypassed with hybrid-type HL.

4. Discussion

This paper proposes to use LD and HD as building blocks of fractal-like and hybrid-type HL with the goal of attaining a CTE range that can be theoretically unbound, and if desired this boost can be obtained with no penalty in elastic stiffness. Experimental results with specifics illustrated in Figs. 3–5, are reported in Fig. 7c and d and provide validation to the trends obtained via closed-form expressions presented in Section 2 and numerically via AH. Thermo-elastic properties of fractal-like HL in Fig. 6 demonstrate that the addition of only one order of hierarchy enlarges the CTE tunability by 66%, which is up to five times higher than what can be obtained through a change in skew angle. On the other hand,

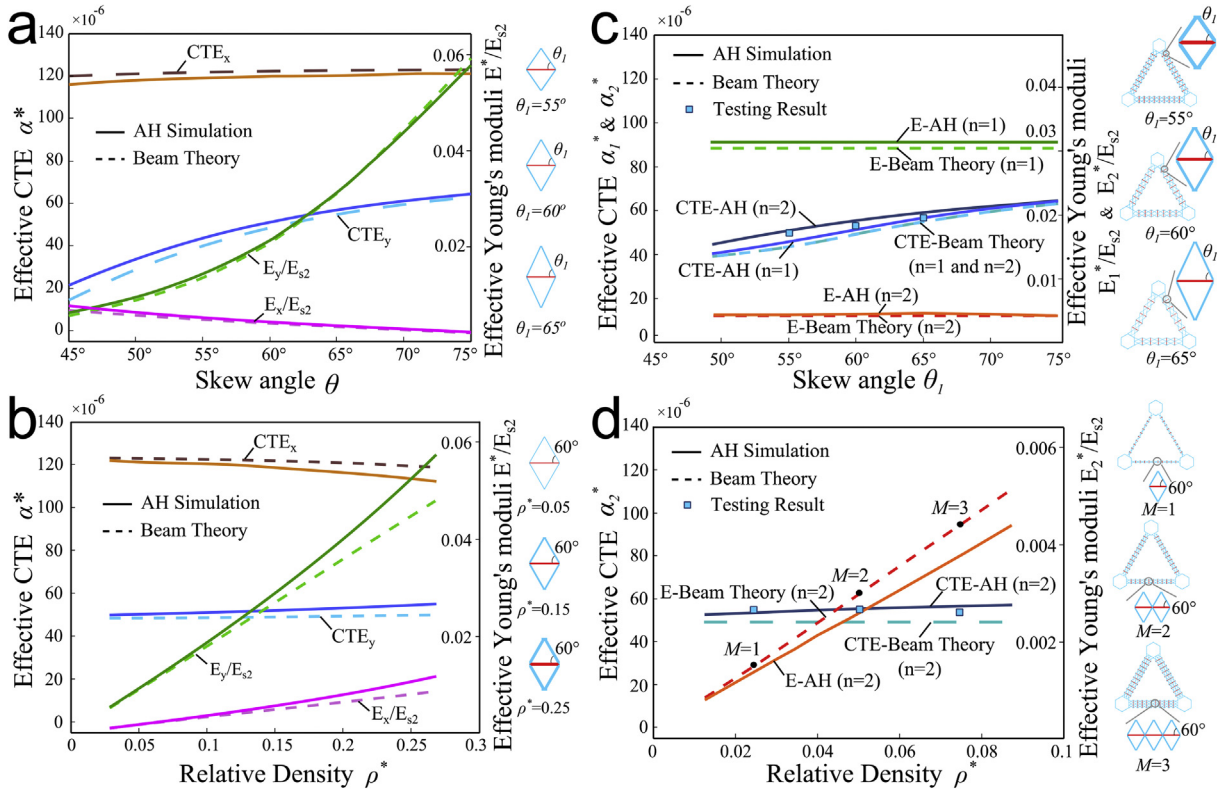

Fig. 7. Visualization of properties coupling and decoupling for LD unit and hierarchical lattices. A change in skew angle (a) and relative density (b) in LD affects both thermal (α_x^* and α_y^*) and elastic properties (E_x^*/E_{s2}^* and E_y^*/E_{s2}^*)). On the other hand for hybrid-type HL (c and d), α_1^* and α_2^* of the first and the second order, as well as their effective Young's modulus, are tuned to preserve constant either the Young's modulus (E_{1y}^*) in (c) or the CTE (α_2^*) in (d). This is achieved in (c) through changing both the skew angle of the first order, θ_1, and t_1/l_1, and in (d) by keeping these parameters constant and varying the relative density of the second order, ρ_2^*/ρ_s^*.

hybrid-type HL allows an increase in structural efficiency equal to 0.0585 of 20.6% (Fig. 6 at $n = 2$) with respect to that of fractal-like HL (0.0485) at the identical order. Validated models of hybrid-type HL suggest that concepts with higher orders can offer much larger CTE tunability than stretch-dominated lattice benchmarks [18] and superior mechanical performance than baseline concepts that are bend-dominated [26], in addition to their decoupled, planar isotropic thermo-elastic properties.

To compare the thermo-elastic performance of fractal-like and hybrid-type HL ($n \leq 5$) with the existing ones, in particular L-Concept [26] and S-Concept [18], we plot in Fig. 8a bars of their specific stiffness, a measure of structural efficiency, and of ΔCTE, the CTE tunability defined as the maximum range of CTE values a concept can offer. The magnitude of a given performance metric is represented by the bar height. All concepts are compared on an equal basis, as they are generated from the same pair of materials (PTFE and acrylic). With respect to the (orange) bars of CTE tunability in Fig. 8a, ΔCTE is calculated for each concept and for a given value of Young's modulus, which is representatively considered here as 1 MPa. From the bar rises, we gather that fractal-like HL dominates with the largest CTE range ($534 \times 10^{-6}/°C$), whereas ΔCTE for the S-Concept is the smallest ($169 \times 10^{-6}/°C$). ΔCTE for hybrid-type HL ($331.1 \times 10^{-6}/°C$) is as high as that of L-Concept ($332.6 \times 10^{-6}/°C$), which is claimed to provide unbounded ΔCTE. This is quite unique, as the L-Concept relies on bend-dominated cells, whereas the proposed hybrid-type HL can obtain a similar result using a much stiffer structure. Similarly with respect to structural efficiency (green bars), Fig. 8a provides a visual comparison of the specific stiffness of each concept for a representative CTE value that is here assumed as half the average of the materials' CTE ($47.5 \times 10^{-6}/°C$). From the bars, we observe that fractal-like HL has the highest specific stiffness in the y-direction (349.2 KPa $\times$ m^3/Kg) followed by hybrid-type HL (116.5 KPa $\times$ m^3/Kg), both of which outperform the existing concepts. More specifically, focusing on planar isotropic materials, hybrid-type HL provides a 42% increase in structural efficiency compared to the stiff, yet dense, S-Concept (82 kPa $\times$ m^3/Kg), while demonstrating twice the specific stiffness of the L-Concept (51.7 KPa $\times$ m^3/Kg).

A more comprehensive comparison of the concepts is illustrated in Fig. 8b, where CTE tunability is plotted versus specific stiffness. The curves are created from a parametric study of the unit cells, where the skewness angle and the thickness-to-length ratio are the active variables for given materials. Hybrid-type and fractal-like HL are compared with L-Concept and S-Concept, the benchmarks. While both high- and low-CTE cases (Fig. 6) can be plotted, Fig. 8b displays only the low-CTE concepts which are sufficient to capture the potential of hierarchical lattices. We recall that, in this low-CTE case, ΔCTE is defined by the range between the lowest CTE value of a given low-CTE concept, at the calculated structural efficiency, and the CTE of the solid material with lower thermal expansion (i.e. $67 \times 10^{-6}/°C$ of acrylic).

While S- and L-Concepts show curves that describe the change of ΔCTE with structural efficiency, hybrid-type and fractal-like HL are represented by two domains (blue for hybrid-type HL and green for fractal-like HL). These shaded regions represent the possible set of curves that are obtained with varying hierarchical orders. For both cases, the first hierarchical order that makes up the concept ($n = 1$ for fractal-like HL and $n = 2$ for hybrid-type HL) provides the most optimal curve (closest to the top-right corner). The following hierarchical orders (the second for fractal-like HL, and the third for hybrid-type HL) provide the least optimal curve, while higher orders lie in between. Higher hierarchical orders are predicted to

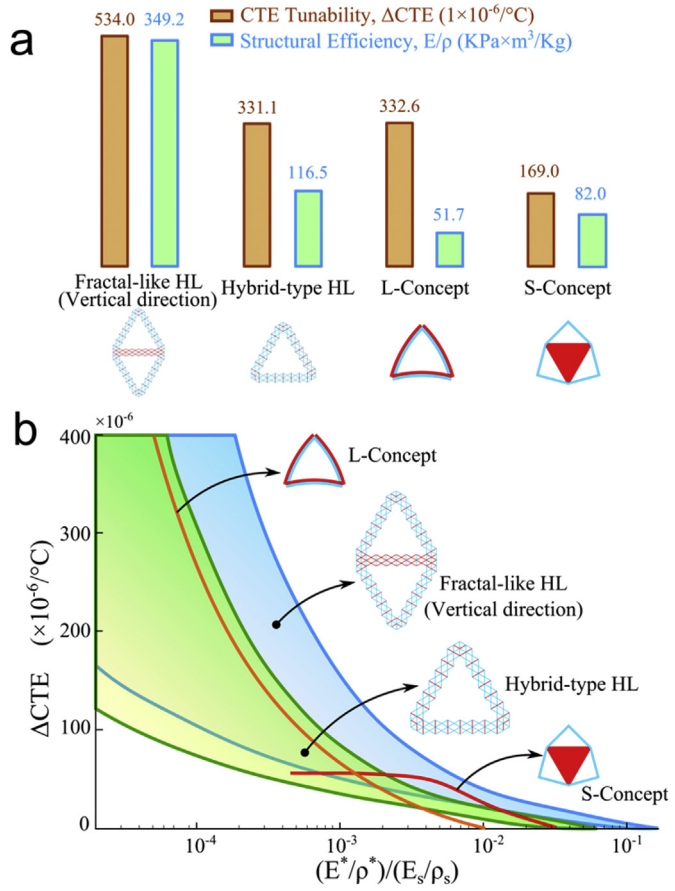

Fig. 8. (a) Comparison of proposed and existing bi-material concepts on the basis of (i) CTE tunability (ΔCTE = Max CTE − Min CTE) for prescribed stiffness of 1 MPa, visualized as orange bars, and (ii) specific stiffness (Young's modulus/Density: E/ρ) for given CTE (47.5×10^{-6}/°C), in green. (b) CTE tunability plotted versus structural efficiency of existing concepts along with hybrid-type and fractal-like HL for increasing hierarchical order ($n = 1, 2, \ldots$). Results are obtained from a parametric study of unit cell geometry, where the list of possible sets of properties for each concept are sorted by increasing structural efficiency, and then grouped based on a range of similar values of E/ρ. The minimum CTE value is selected from each group to calculate ΔCTE for a given E/ρ. This value, the median structural efficiency of each group, is plotted as a point on the graph with the corresponding ΔCTE value on the ordinate axis. (For interpretation of the references to colour in this figure legend, the reader is referred to the web version of this article.)

approach the curve of the first order ($n = 1$ for fractal-like HL and $n = 2$ for hybrid-type HL) with increasing n.

In general, Fig. 8b shows a Pareto-front for the existing concepts, thus showing trade-offs between metrics: an attempt of increasing structural efficiency results in a reduced ΔCTE. This trade-off is not only influenced by the relation between geometric parameters and effective properties, but also by the design requirements. For example, the L-Concept is the ideal candidate to attain large CTE tunability, whereas the S-Concept is ideal for structural efficiency, as both are designed for different specifications. When considering the concepts presented in this paper, a better overall performance can be observed compared to the existing baselines. The curves derived from both fractal-like and hybrid-type HL are offsets of the L- and S-Concept toward the top right corner on the figure, where both high CTE tunability and high structural efficiency are achieved; hence their domains show higher potential of hierarchical lattices to attain better trade-offs between ΔCTE and E/ρ.

While the work here presented show promises for planar lattices, the strategy can be applied also to 3D hierarchical concepts. Nevertheless, their potential should always be confronted with the capabilities of current practices. For example, while the concepts are scale independent and material selection free, increasing the order of structural hierarchy has to account for the limits that a given manufacturing process poses [6]. The fabrication of hierarchical structures can be highly time consuming, and to the best of authors' knowledge, only structures with up to three orders of hierarchy have been physically realized, even recently, such as multi-material shape memory structures (two orders) [36] and multiscale metallic metamaterials which feature three orders of hierarchy [6]. Given the fast development of multiple material additive manufacturing [37,38], we can infer that higher level of hierarchy in dual material lattices might be achieved in the near future. In addition, while thermal expansion and stiffness have been here investigated, other structural properties, such as yield strength and toughness, might not perform equally well in practice as adding hierarchy alone reduces strength further due to high stress concentrations that stem at the joints of dissimilar materials [30].

5. Conclusion

In this paper, stretch-dominated bi-material unit cells with low- and high-CTE have been proposed as diamond shaped building blocks of hierarchical lattices with the goal of improving CTE tunability and structural performance, as well as allowing separate tuning of their thermo-elastic properties. Through simulations, derived closed-form expressions and experiments on fabricated proof-of-concepts, we have shown that hybrid-type HL architecture including those made of self-repeating unit cells, i.e. fractal-like HL, can be tailored to concurrently provide high specific stiffness and theoretically unbounded CTE tunability with CTE values ranging from large positive, zero to large negative. The hallmark of fractal-like and hybrid-type HL is that they can reduce the penalty that an increase in ΔCTE will generate on the elastic properties, so as to obtain the best compromise out of them. In addition, their stretch-dominated behaviour provides higher specific stiffness than existing concepts that are bend-dominated. Another benefit of hybrid-type HL is that they can be exploited to decouple initially coupled thermo-elastic properties so as to provide the individual property tailoring that current concepts have not been proven to attain yet. The strategy presented in this work can pave the way to the multifunctional design of bi-material hierarchical lattices with properties that can be independently tuned and exploited to the most of their potential. It can thus be extended to potentially address other conflicting properties to finally generate trade-off solutions for multifunctional applications, including thermal expansion control, MEMS, biomedical sensors and space optical systems.

Funding

This work was supported by the Natural Sciences and Engineering Research Council of Canada (grant number 462203-13).

Acknowledgements

The authors gratefully acknowledge the technical support of Mr. Daniel Fraschetti who assisted in conducting the experiments. Hang Xu also gratefully acknowledges financial support from the China Scholarship Council [File No. 201306020030].

Appendix A. Supplementary data

Supplementary data related to this article can be found at http://dx.doi.org/10.1016/j.actamat.2017.05.059.

References

[1] M.F. Ashby, Y.J.M. Bréchet, Designing hybrid materials, Acta Mater. 51 (2003) 5801–5821.
[2] N. Palumbo, C. Smith, W. Miller, K. Evans, Near-zero thermal expansivity 2-D lattice structures: performance in terms of mass and mechanical properties, Acta Mater. 59 (2011) 2392–2403.
[3] S. Arabnejad, B. Johnston, M. Tanzer, D. Pasini, Fully porous 3D printed titanium femoral stem to reduce stress-shielding following total hip arthroplasty, J. Orthop. Res. (2016) 1–10.
[4] N. Yamamoto, E. Gdoutos, R. Toda, V. White, H. Manohara, C. Daraio, Thin films with ultra-low thermal expansion, Adv. Mater. 26 (2014) 3076–3080.
[5] M.G. Lee, J.W. Lee, S.C. Han, K. Kang, Mechanical analyses of "Shellular", an ultralow-density material, Acta Mater. 103 (2015) 595–607.
[6] X. Zheng, W. Smith, J. Jackson, B. Moran, H. Cui, D. Chen, J. Ye, N. Fang, N. Rodriguez, T. Weisgraber, C.M. Spadaccini, Multiscale metallic metamaterials, Nat. Mater. 15 (2016) 1100–1106.
[7] T.J. Lu, H.A. Stone, M.F. Ashby, Heat transfer in open-cell metal foams, Acta Mater. 46 (1998) 3619–3635.
[8] P. Wang, J. Shim, K. Bertoldi, Effects of geometric and material nonlinearities on tunable band gaps and low-frequency directionality of phononic crystals, Phys. Rev. B Condens. Matter Mater. Phys. 88 (2013) 014304.
[9] S.A. Khanoki, D. Pasini, Multiscale design and multiobjective optimization of orthopedic hip implants with functionally graded cellular material, J. Biomech. Eng. 134 (2012) 031004.
[10] Z. Wang, L. Jing, J. Ning, L. Zhao, The structural response of clamped sandwich beams subjected to impact loading, Compos. Struct. 93 (2011) 1300–1308.
[11] Q. Wang, J.A. Jackson, Q. Ge, J.B. Hopkins, C.M. Spadaccini, N.X. Fang, Lightweight mechanical metamaterials with tunable negative thermal expansion, Phys. Rev. Lett. 117 (2016) 175901.
[12] K. Wei, H. Chen, Y. Pei, D. Fang, Planar lattices with tailorable coefficient of thermal expansion and high stiffness based on dual-material triangle unit, J. Mech. Phys. Solids 86 (2016) 173–191.
[13] D.G. Gilmore, Spacecraft Thermal Control Handbook: Fundamental Technologies, Aerospace Press, United States, 2002.
[14] J.A. Monroe, D. Gehring, I. Karaman, R. Arroyave, D.W. Brown, B. Clausen, Tailored thermal expansion alloys, Acta Mater. 102 (2016) 333–341.
[15] S. Naficy, R. Gately, R. Gorkin, H. Xin, G.M. Spinks, 4D printing of reversible shape morphing hydrogel structures, Macromol. Mater. Eng. 302 (2017) 1600212.
[16] Y. Mao, Z. Ding, C. Yuan, S. Ai, M. Isakov, J. Wu, T. Wang, M.L. Dunn, H.J. Qi, 3D printed reversible shape changing components with stimuli responsive materials, Sci. Rep. 6 (2016) 24761.
[17] Z. Yong, C. Tzu-Hsuan, A review of microelectromechanical systems for nanoscale mechanical characterization, J. Micromech. Microeng. 25 (2015) 093001.
[18] C.A. Steeves, S.L. dos Santos e Lucato, M. He, E. Antinucci, J.W. Hutchinson, A.G. Evans, Concepts for structurally robust materials that combine low thermal expansion with high stiffness, J. Mech. Phys. Solids 55 (2007) 1803–1822.
[19] J. Lehman, R.S. Lakes, Stiff, strong, zero thermal expansion lattices via material hierarchy, Compos. Struct. 107 (2014) 654–663.
[20] G. Jefferson, T.A. Parthasarathy, R.J. Kerans, Tailorable thermal expansion hybrid structures, Int. J. Solids Struct. 46 (2009) 2372–2387.
[21] O. Sigmund, S. Torquato, Composites with extremal thermal expansion coefficients, Appl. Phys. Lett. 69 (1996) 3203–3205.
[22] O. Sigmund, S. Torquato, Design of smart composite materials using topology optimization, Smart Mater. Struct. 8 (1999) 365–379.
[23] H. Xu, D. Pasini, Structurally efficient three-dimensional metamaterials with controllable thermal expansion, Sci. Rep. 6 (2016) 34924.
[24] J. Lehman, R. Lakes, Stiff, strong zero thermal expansion lattices via the Poisson effect, J. Mater. Res. 28 (2013) 2499–2508.
[25] J.B. Hopkins, Y. Song, H. Lee, N.X. Fang, C.M. Spadaccini, Polytope sector-based synthesis and analysis of microstructural architectures with tunable thermal conductivity and expansion, J. Mech. Des. 138 (2016) 051401.
[26] R. Lakes, Cellular solid structures with unbounded thermal expansion, J. Mater. Sci. Lett. 15 (1996) 475–477.
[27] J. Lehman, R. Lakes, Stiff lattices with zero thermal expansion and enhanced stiffness via rib cross section optimization, Int. J. Mech. Mater. Des. 9 (2013) 213–225.
[28] R. Lakes, Materials with structural hierarchy, Nature 361 (1993) 511–515.
[29] A. Vigliotti, D. Pasini, Mechanical properties of hierarchical lattices, Mech. Mater. 62 (2013) 32–43.
[30] S. Banerjee, On the mechanical properties of hierarchical lattices, Mech. Mater. 72 (2014) 19–32.
[31] H.E.M. Hunt, The mechanical strength of ceramic honeycomb monoliths as determined by simple experiments, Chem. Eng. Res. Des. 71a (1993) 257–266.
[32] N.E.R. Romijn, N.A. Fleck, The fracture toughness of planar lattices: imperfection sensitivity, J. Mech. Phys. Solids 55 (2007) 2538–2564.
[33] D. Pasini, Shape transformers for material and shape selection of lightweight beams, Mater. Des. 28 (2007) 2071–2079.
[34] D. Pasini, Shape and material selection for optimizing flexural vibrations in multilayered resonators, J. Microelectromech. Syst. 15 (2006) 1745–1758.
[35] D. Pasini, D.J. Smith, S.C. Burgess, Selection of arbitrarily scaled cross-sections in bending stiffness design, Proc. Inst. Mech. Eng. Part L 217 (2003) 113–125.
[36] Q. Ge, A.H. Sakhaei, H. Lee, C.K. Dunn, N.X. Fang, M.L. Dunn, Multimaterial 4D printing with tailorable shape memory polymers, Sci. Rep. 6 (2016) 31110.
[37] M. Vaezi, S. Chianrabutra, B. Mellor, S. Yang, Multiple material additive manufacturing – Part 1: a review, Virtual Phys. Prototyp. 8 (2013) 19–50.
[38] F. Momeni, S.M. Mehdi Hassani, N.,X. Liu, J. Ni, A review of 4D printing, Mater. Des. 122 (2017) 42–79.